PLANETARY SCIENCE

Upper mantle structure of Mars from InSight seismic data

Amir Khan[1,2]*, Savas Ceylan[1], Martin van Driel[1,3], Domenico Giardini[1], Philippe Lognonné[4], Henri Samuel[4], Nicholas C. Schmerr[5], Simon C. Stähler[1], Andrea C. Duran[1], Quancheng Huang[5], Doyeon Kim[5], Adrien Broquet[6,7], Constantinos Charalambous[8], John F. Clinton[9], Paul M. Davis[10], Mélanie Drilleau[11], Foivos Karakostas[5], Vedran Lekic[5], Scott M. McLennan[12], Ross R. Maguire[5], Chloé Michaut[13,14], Mark P. Panning[15], William T. Pike[8], Baptiste Pinot[11], Matthieu Plasman[4], John-Robert Scholz[16], Rudolf Widmer-Schnidrig[17], Tilman Spohn[18], Suzanne E. Smrekar[15], William B. Banerdt[15]

For 2 years, the InSight lander has been recording seismic data on Mars that are vital to constrain the structure and thermochemical state of the planet. We used observations of direct (*P* and *S*) and surface-reflected (*PP*, *PPP*, *SS*, and *SSS*) body-wave phases from eight low-frequency marsquakes to constrain the interior structure to a depth of 800 kilometers. We found a structure compatible with a low-velocity zone associated with a thermal lithosphere much thicker than on Earth that is possibly related to a weak *S*-wave shadow zone at teleseismic distances. By combining the seismic constraints with geodynamic models, we predict that, relative to the primitive mantle, the crust is more enriched in heat-producing elements by a factor of 13 to 20. This enrichment is greater than suggested by gamma-ray surface mapping and has a moderate-to-elevated surface heat flow.

The Interior Exploration Using Seismic Investigations, Geodesy and Heat Transport (InSight) mission (*1*) touched down on Mars in Elysium Planitia (*2*) at the end of 2018 and has been acquiring high-quality seismic data with the Seismic Experiment for Interior Structure (SEIS) instrument (*3*) since early 2019 (*4, 5*). SEIS's main instrument is a three-component very-broadband seismometer (*6*), and to date (sol 676), >1000 distinct seismic events have been identified by the Marsquake Service (MQS) (*7*). A primary goal of the InSight mission (*1*) is to image the interior structure of Mars from observations of seismic events and to use this to improve our understanding of its formation and evolution.

The compilation of travel-time tables of seismic body waves by Jeffreys and Bullen (*8*) was of fundamental importance for establishing the first radial average structure of Earth's interior. Earth's seismic velocity structure has been constrained by a plethora of seismic observations including body waves, surface waves, and normal modes (*9–12*). However, replicating this progress on the Moon has been more difficult. For the Moon, strong scattering in the shallow parts of the lunar crust has largely limited seismic observations to the main *P*- and *S*-wave arrivals (*13*) and core reflections (*14, 15*), from which averaged radial seismic

profiles of the crust, mantle, and core could be deduced (*16*). Relative to the four-station seismic array that operated on the Moon, travel-time inversions on Mars are complicated because accurate epicentral distance and origin-time measurements of marsquakes are difficult to obtain with only one seismic station. Only event distance can be estimated from arrival-time measurements of direct *P*- and *S*-waves (*5*). To obtain information on interior structure, we need observations of additional seismic phases such as planet-circling surface waves (*17, 18*), normal modes (*19, 20*), or reflected and refracted body waves that have interacted with the surface or internal boundaries. As we have yet to positively identify planet-circling waves or normal modes on Mars, we used observations of *P*- and *S*-wave differential travel-time measurements together with surface-reflected body-wave phases *PP*, *PPP*, *SS*, and *SSS* (fig. S1) to jointly invert for both epicentral distance and interior structure. This strategy allows us to construct a quantitative model of the seismic velocity structure of the martian mantle.

Marsquakes have been divided into two main categories based on their frequency content. The low-frequency (LF) events have energy dominantly below 1 Hz, and high-frequency (HF) events have energy dominantly above 1 Hz (*5, 7*). InSight has recorded far more HF

events, and these events often lack clearly identifiable *P*- and *S*-wave arrivals and polarizations. Here, we focused on eight high-quality LF events of the 43 recorded to date by InSight (*21*), labeled by mission sol of occurrence and sublabeled alphabetically for sols with more than one event: S0167b, S0173a, S0185a, S0189a, S0235b, S0325a, S0407a, and S0484b. Each of these events has a high signal-to-noise ratio with identifiable *P*- and *S*-waves, which allows for epicentral distance estimation (*7*). We determined the back azimuth of three events (S0173a, S0235b, and S0325a) from polarization and found that all were located in the Cerberus Fossae region (*7*). These eight events occurred in the distance range ~25° to 75° and had moment magnitudes M_W between 3.0 and 4.0 (*7*).

An example broadband-filtered seismogram from marsquake event S0235b is shown in Fig. 1A and includes our picks of the direct *P*- and *S*-wave arrivals. Marsquake waveforms are characterized by codas produced by scattering (*4, 5*), which, like their lunar seismogram counterparts, complicate the identification of seismic body-wave phases. Consequently, we do not identify seismic arrivals directly in the time series, but instead use narrowband-filtered time-domain envelopes (Fig. 1B) called filter banks (*6*). Figure 1B shows a zoom-in around the main *P*- and *S*-wave arrivals for event S0235b and our identification of surface-reflected body-wave phases *PP*, *PPP*, and *SS* that were made on the filter banks (bold black lines). We made our picks on the envelope peaks rather than the phase onsets because arrival onsets are more difficult to discern for the later-arriving seismic phases. Filter banks for the eight LF events considered here are shown in fig. S9.

To provide an independent verification of the filter bank–based picks, we used complementary methods for the identification of seismic phases. These include (i) polarization filtering and vespagrams, and (ii) waveform matching (*6*). Despite the independent nature of the three analysis methods, our picks (table S4) are consistent within the overlapping uncertainties as illustrated in fig. S9. To ensure that the arrivals identified in the envelopes were not due to noise, we compared the observed waveforms to the pulse shape of the direct *P*- and *S*-wave arrivals. As we expected for multiply reflected body waves, the waveforms we observed are consistent with shifts

[1]Institute of Geophysics, ETH Zürich, Zürich, Switzerland. [2]Physik-Institut, University of Zürich, Zürich, Switzerland. [3]Mondaic AG, Zypressenstrasse 82, 8004 Zürich, Switzerland. [4]Université de Paris, Institut de Physique du Globe de Paris, CNRS, Paris, France. [5]Department of Geology, University of Maryland, College Park, MD, USA. [6]Lunar and Planetary Laboratory, University of Arizona, Tucson, AZ 85721, USA. [7]Université Côte d'Azur, Observatoire de la Côte d'Azur, CNRS, Laboratoire Lagrange, Nice, France. [8]Department of Electrical and Electronic Engineering, Imperial College London, London, UK. [9]Swiss Seismological Service, ETH Zürich, Zürich, Switzerland. [10]Department of Earth, Planetary, and Space Sciences, University of California, Los Angeles, CA, USA. [11]Institut Supérieur de l'Aéronautique et de l'Espace SUPAERO, Toulouse, France. [12]Department of Geosciences, Stony Brook University, Stony Brook, NY, USA. [13]Institut Universitaire de France, Paris, France. [14]Laboratoire de Géologie, Terre, Planétes, Environnement, Lyon, France. [15]Jet Propulsion Laboratory, California Institute of Technology, Pasadena, CA, USA. [16]Max Planck Institute for Solar System Research, Göttingen, Germany. [17]Black Forest Observatory, Institute of Geodesy, University of Stuttgart, Stuttgart, Germany. [18]International Space Science Institute, Bern, Switzerland.
*Corresponding author. Email: akhan@ethz.ch

in phase of 90° and 180° for *PP/SS* and *PPP/SSS*, respectively (*6*). On the basis of absence of surface waves and dispersion in the LF seismograms, we assumed that the events occurred below the crust-mantle interface (*5, 22*) at a depth of 50 km. We found that varying assigned event depth in the range 50 to 70 km produced little difference in inversion results. We note that for some events, possible depth phases are discernable (Fig. 1B) but are not considered in the inversion.

We used the travel-time picks based on the visual inspection of filter banks (table S4, bold numbers) as our preliminary differential travel-time dataset to simultaneously invert for epicentral distance (Δ) and elastic seismic wave velocity structure (*18, 23*). We modeled Mars as a spherically symmetric planet, although we acknowledge that it varies laterally in crustal thickness (*24, 25*) and possibly in seismic properties (*20, 26*). Global and regional synthetic seismograms that we computed for one- and three-dimensional (1D, 3D) Mars models (*23, 26*) yielded generally small travel-time differences between 1D and 3D models for the direct *P*- and *S*-wave arrivals (<3 s). Thus, picking uncertainty (5 to 10 s) should be larger than what we expect for 3D effects. This might not be the case for the multiply reflected waves. For instance, 3D effects could potentially be more pronounced for the surface-reflected phases because they travel in the more heterogeneous shallow structure beneath Elysium Planitia (*1, 4*).

We carried out two separate inversions to determine interior structure using a seismic and a geophysical parameterization (*6*). The seismic parameterization is based on *P*- and *S*-wave velocities in a layered planet model (*23*), whereas the geophysical parameterization (*18, 27*) relies on an unified description of phase equilibria, seismic properties, and thermochemical parameters. We assumed a homogeneous bulk composition derived from the martian meteorites (*28*) and computed *P*- and *S*-wave velocities as a function of temperature, composition, and pressure using Gibbs free energy minimization (*29*). On the basis of stagnant-lid models that include a crust enriched in heat-producing elements (*30–33*), we parameterized the martian geotherm using variable conductive crustal and lithospheric geotherms for which the underlying mantle can be assumed to be adiabatic. The exact nature of the crustal geotherm is less important here because we relied on a seismic parameterization of the crust (*6*). We computed mantle adiabats (isentropes) self-consistently from the entropy of the lithology at the pressure and temperature of the bottom of the thermal lithosphere (*6*). To solve the inverse problem (*6*), we used a stochastic sampling algorithm (*34*) that produces a suite of models that fit the differential travel times, within uncertainty, and enable estimates of model
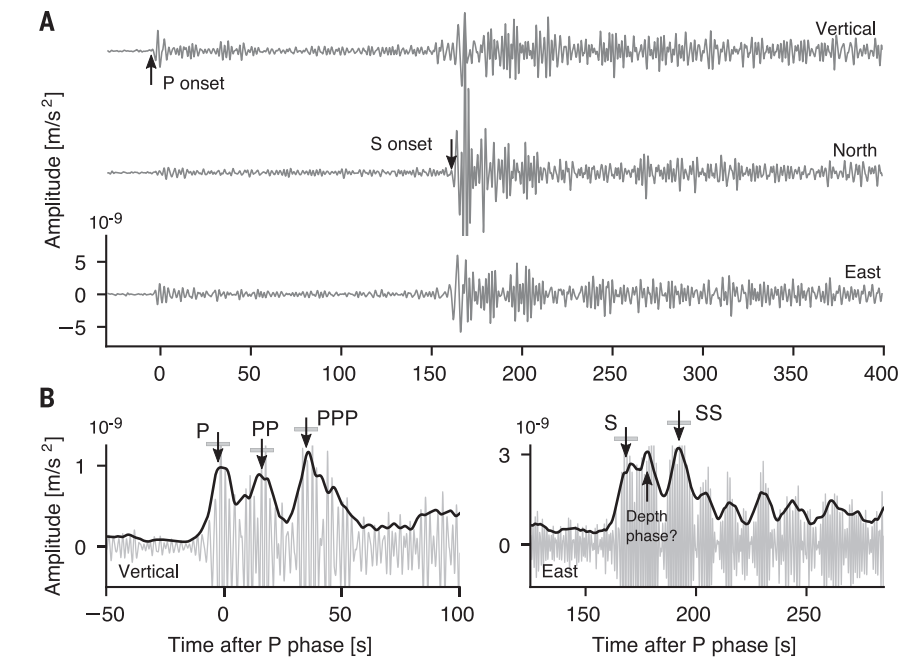

Fig. 1. Marsquake recorded by the InSight seismometer. (**A**) Three-component broadband-filtered (1.5 to 8 s) seismogram of event S0235b. The main direct *P*- and *S*-wave arrivals are indicated by the vertical arrows. (**B**) Close-up view of the *P*-wave (left) and *S*-wave (right) arrivals, showing the direct and surface-reflected body waves (*PP*, *PPP*, and *SS*). Because arrival onsets are less palpable for the surface-reflected phases, arrivals are picked on the peak rather than the onset (arrows). The arrival of a possible depth phase is also marked. Bold black lines indicate the time-domain envelopes that are used for picking phase arrivals. The *P*- and *S*-wave envelopes are filtered at 2 s and 1.4 s, respectively, and are 0.5 octave wide on either side. Horizontal gray bars indicate the measurement uncertainty on the picks.

parameter uncertainty. In total we sampled 10^5 models, of which ~10^4 were retained to ensure model independence.

We inverted for radial *P*- and *S*-wave velocity and geothermal profiles (Fig. 2, A and B), using both the geophysical parameterization (red and blue models) and the seismic parameterization (gray-shaded models). The seismic velocity profiles we obtained from both inversions are very similar, with slightly wider posterior model parameter ranges in the case of the seismic parameterization. This reflects the inclusion of mineral physics information in the geophysical parameterization. On the basis of ray path geometry and sensitivity (Fig. 2C), we found that the differential travel-time data constrained the structure to 800-km depth, with sensitivity below ~500 km provided primarily by the two events located at Δ > 60° (S0185a and S0167b). Below 800-km depth, the distribution of inverted profiles starts to resemble the prior *P*- and *S*-wave velocity distributions (fig. S10, gray-shaded areas), signaling loss of resolution. Comparison of prior (fig. S13) and posterior (Fig. 2, A and B) distributions of geothermal and *P*- and *S*-wave velocity profiles based on the geophysical parameterization confirms that the differential travel-time data constrain upper mantle structure. For both parameterizations, *S*-wave velocity is

better constrained than *P*-wave velocity, which reflects the more abundant number of *S*-wave picks relative to *P*-wave picks. We found good agreement between the inverted epicentral distances for both parameterizations (fig. S11), with slightly wider Δ distributions for the seismic parameterization because of the broader velocity distributions. We focus on the implications of the geophysical parameterization because it provides a good fit to the observations (Fig. 2, D and E).

We grouped the geotherms, including lithospheric geothermal gradients (Fig. 2B, inset), and seismic wave velocity profiles into families according to lithospheric thickness (Z_{lit}): Z_{lit} < 400 km (fig. S13, green models), Z_{lit} = 400 to 500 km (blue models), and Z_{lit} = 500 to 600 km (red models). We found that only models that group in a Z_{lit} range of 400 to 600 km (blue and red models), corresponding to a thermal gradient between 1.6 and 2.5 K/km (mantle potential temperatures between 1600 and 1700 K), fit the data. These thermal gradients are consistent with those obtained on the basis of radar observations of the faint lithospheric flexure beneath the north polar cap (1.3 to 3.2 K/km), which constrains the thermal state of the present-day lithosphere (*35*).

Our crustal velocity models (Fig. 2A, insets) include an upper-crustal low-velocity layer with

Fig. 2. Summary of Mars' upper mantle structure.
(**A** and **B**) Inverted S- and P-wave velocity and geothermal profiles. Colored (red and blue) and gray-shaded models are obtained from the geophysical and seismic inversions, respectively. Insets show the distribution of sampled crustal S- and P-wave velocity structure and lithospheric geothermal gradients (dT/dz), respectively. Profiles are color-coded according to lithospheric thickness: 400 to 500 km (blue) and 500 to 600 km (red). The lithospheric thermal gradient is determined from the temperature at the crust-mantle interface and at the bottom of the lithosphere and from the difference in depth between the two points. For comparison, prior sampled models are shown in fig. S13. Gray-shaded contours in (A) indicate the 50%, 75%, and 90% credible intervals computed from the distribution of models inverted using a purely seismic parameterization (6). (**C**) Body-wave ray path geometry for the eight events (labeled S0167b, S0185a, etc.) considered in this study. Color bar denotes ray path density (i.e., number of rays passing through a given area)

based on inverted models shown in (A), which explains the diffuseness of ray paths and source locations. The column to the left of "InSight" shows radial sensitivity, computed as the integrated ray path density with epicentral distance. (**D** and **E**) Differential body-wave travel-time misfits for all sampled models shown in (A). Green and purple lines denote differential travel times computed using the inverted models; squares and circles indicate the observations including error bars. For the travel-time calculations performed here, we always pick the first arrival. See fig. S14 for a more detailed version of the differential travel-time misfit.
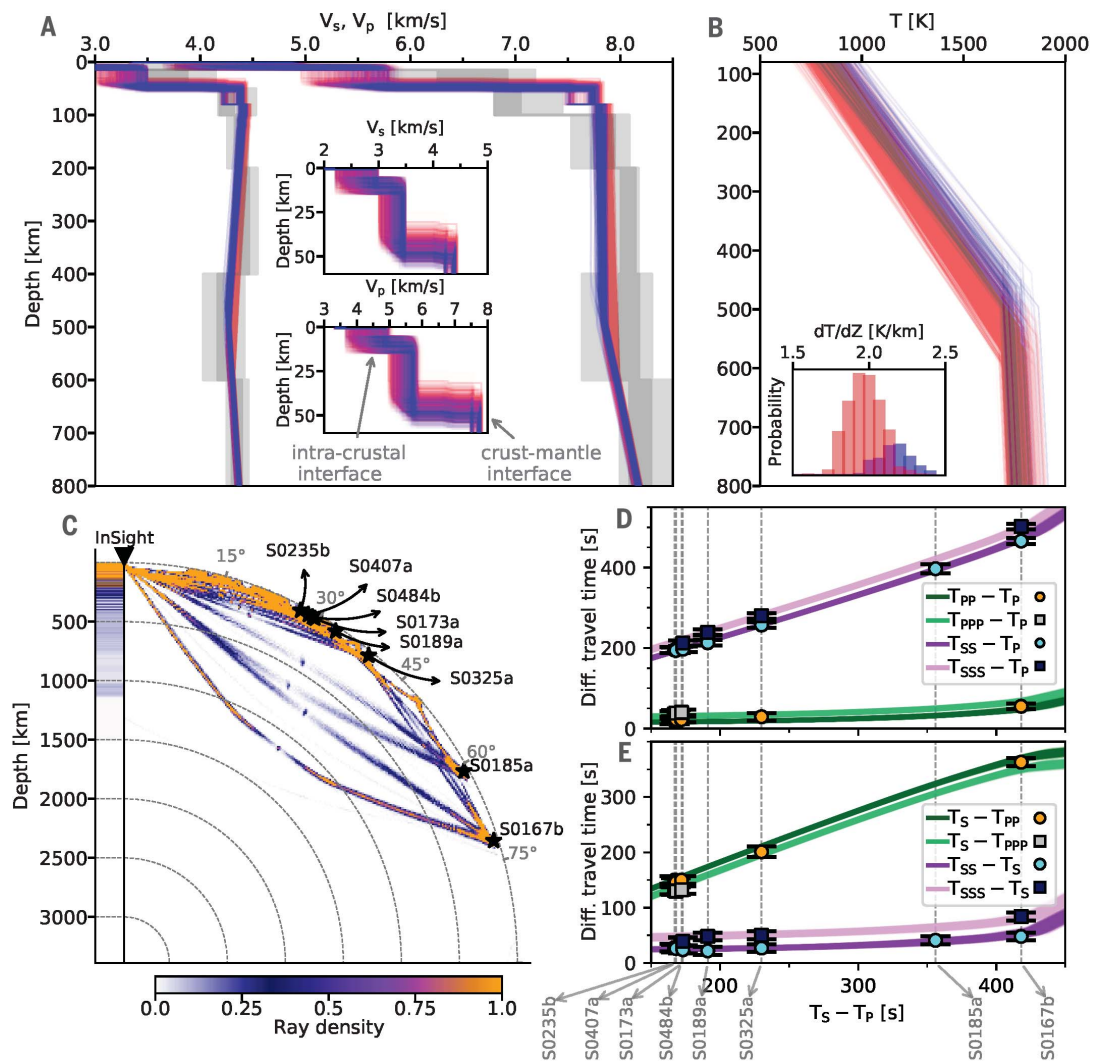
S- and P-wave velocities in the ranges 2 to 3 km/s and 3.5 to 5 km/s, respectively, separated from the lower crust by an intracrustal discontinuity around 5- to 10-km depth, which had been observed previously (4), and a larger discontinuity around 30- to 50-km depth that could be the crust-mantle interface. Lateral variations in crustal structure can result in differences between near-station structure and profiles inverted from our differential travel-time dataset, which averages structure across a wide geographic region, yet may not be entirely representative of the average structure of Mars. The crustal discontinuities beneath the InSight lander are discussed in more detail in (36).

At greater depth, the lithospheric structure is characterized by constant negative S- and neutral-to-positive P-wave velocity gradients, respectively, to depths of 400 to 600 km. The

S-wave velocity decrease, an inherent feature of the models and consistent with the data, is followed by an increase to 800-km depth. This behavior defines an S-wave low-velocity zone (LVZ) in the martian upper mantle. The LVZ results from the large thermal gradient across the lithosphere that arises when a relatively thick stagnant conductive thermal boundary layer sits on top of a convective mantle, as previously postulated (37). A possible manifestation of an LVZ is the presence of a weak S-wave shadow zone at epicentral distances of ~40° to 60°. There is no equivalent LVZ for compressional waves because P-wave velocity is less affected by temperature. The LVZ on Mars results from the decrease in seismic velocity associated with increasing temperature with depth dominating over the opposing increase in seismic velocity associated with the

increase in pressure with depth. Other mechanisms such as fluid and melt in the asthenosphere (38) and redox effects (39) are also thought to play a role in shaping Earth's LVZ (40), but we lack the resolution to address these issues.

To provide an observational constraint on the strength and extent of the LVZ, we considered the alignment of the seismic traces (fig. S9A) to qualitatively estimate the S-wave amplitude behavior with distance. From the alignment, we make the following observations: (i) For Δ < 40°, both P- and S-wave arrivals are identifiable (S0235b, S0407a, S0484b, S0173a, S0189a, and S0325a); (ii) for 40° < Δ < 59°, only a P-wave arrival is visible above the background noise on the vertical component, although there is a signal consistent with a low-amplitude S-wave (S0183a); and (iii) for Δ > 59°, P- and

S-wave arrivals are again distinctly visible (S0185a and S0167b). We interpreted the recovery in *S*-wave amplitude as the bottom of the LVZ because the increase in *S*-wave amplitude is commensurate with velocity switching to an increase with depth. This sequence provides tentative observational evidence for a weak *S*-wave shadow zone in the ~40° to 59° epicentral distance range.

We compared the InSight observations to reflectivity synthetics (6) for a range of models covering the inverted blue and red families (Fig. 3). The synthetic relative *S*- to *P*-wave amplitude ratios illustrate the effect of the LVZ and lead us to predict that the *S*- to *P*-wave amplitude ratio falls off with increasing epicentral distance, but stabilizes where the velocity gradient begins to increase with depth. The drop in synthetic relative amplitudes between ~53° and 59° is compatible with the low-amplitude *S*-wave event S0183a (not included in our travel-time inversions) and allows us to revise the event's distance and the models obtained from the travel-time inversion. The colored box (beige and brown) shows the allowed range (~40° to 59°) based on alignment (fig. S9A); the brown portion corresponds to the location (~54° to 59°) for which synthetically predicted amplitudes drop, as observed for S0183a. Comparison with InSight observations (Fig. 3, gray boxes) indicates that the blue model family predicts an amplitude behavior that is in line with the location of both the observed amplitude drop (S0183a) and amplitude increase (S0185a). The red model family would appear to put S0183a (drop) in slight contradiction with the inferred location of S0185a (increase).

The weak *S*-wave shadow zone is based on an absent or low-amplitude *S*-wave from a single event (S0183a), which could potentially arise from the source radiation pattern. However, the relatively long (several minutes) coda that is observed throughout suggests that near-source scattering is substantial and that *S*-wave energy is emitted in all directions. Because the ray paths of the direct and coda *S*-waves are similar, the simultaneous absence of both is best explained by geometrical spreading such as that produced by a shadow zone. Attenuation may also result in additional complexity if the quality factors (*Q*) are strongly depth-dependent, such that the effective attenuation along the path is different for the surface-reflected phases. Our initial observations from the direct phases suggest an effective $Q \approx 200$ to 300 to distances of 45° (4, 5), and a similar value is expected for the surface-reflected phases. Alternatively, if we assume that attenuation increases with depth, the more deeply diving *S*-waves would simply weaken and would therefore be unable to replicate the amplitude effects of a LVZ, as evidenced by S0183a and S0185a.
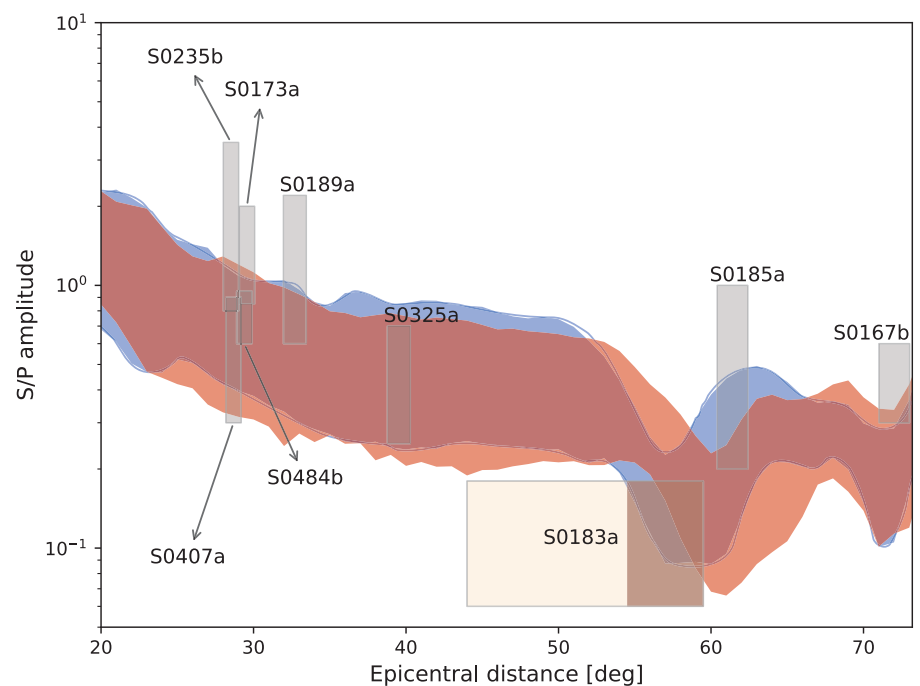

Fig. 3. Seismic amplitude behavior with distance. Blue and red bands show the predicted *S/P* amplitude ratio computed using a range of models covering the inverted blue and red model families (Fig. 2) that correspond to models with lithospheric thicknesses in the ranges 400 to 500 km and 500 to 600 km, respectively. The gray boxes indicate the observed *S/P* amplitude ratio for the events that have been determined from the time-domain envelopes (fig. S9A). The height of the gray boxes indicates the uncertainty on the observed amplitudes, whereas their location and width are based on the inverted epicentral distance distributions (fig. S11), except for S0183a. For S0183a, the widths of the beige and brown boxes show the ranges based on the alignment (fig. S9A) and the synthetically predicted amplitudes, respectively.

The presence of the LVZ has important implications for the thermal evolution of the martian mantle, the formation of the crust, and the planet's surface heat flow. To identify plausible geophysical parameters that pertain to the dynamical evolution of Mars, we computed present-day thermal profiles using a parameterized stagnant-lid mantle and core convection model that simulates 4.5 billion years of planetary evolution (32, 41–43). We explored all relevant geodynamic model parameters in computing the thermal evolution of Mars (6) and compared the resulting present-day lithospheric thermal profiles and crust and lithospheric thicknesses with the models constrained seismically (Fig. 2B).

We found that the seismic results are reproducible by parameterized convection models for a restricted range of geodynamic model parameters. In particular, the models point toward an initially relatively cold state (mantle potential temperature in the range 1630 to 1720 K) and a moderately sluggish mantle (with a reference viscosity $\eta_0 = 10^{20.2}$ to $10^{21.8}$ Pa·s). The bulk heat-producing element (HPE) content of the primitive mantle could be comparable to estimates based on the martian meteorites (28, 44) or 25 to 50% more enriched (45). Moreover, to match the seismic results requires

a crust that is more enriched in HPEs than the primitive mantle by a factor of 13 to 20, leading to an average surface heat flow of 14 to 29 mW/m² — a value that is generally higher than previously estimated (27, 31–33, 46–48). These enrichment levels also call into question models of crustal composition (6, 49, 50). Models that estimate crustal HPE from orbital gamma-ray near-surface mapping (51) predict HPE enrichments relative to the primitive mantle by a factor of no more than 12 (50). Accordingly, deeper crust may mostly consist of petrologically more evolved lithologies, such as those observed at Gale crater and in martian brecciated meteorites (52) and in TES Surface Type 2 (53).

We related mantle thermal structure to surface heat flow using radial models with an average crustal thickness, neglecting regional variations that could vary across the surface of Mars, perhaps by a factor of 2 or more (33, 47). Fortuitously, the area sampled by the seismic data, between Cerberus Fossae and the InSight landing site, has been predicted to be relatively homogeneous in terms of surface heat flow and close to the average planetary value (33). Thus, our approach appears justified given the large uncertainty in current surface heat flow predictions.

As of sol 676, the SEIS instrument has operated at optimal noise conditions during the

martian northern spring and summer between sols 100 and 520 (*1*, *5*). Since then, the average wind speed has increased to a level that would make all but the three largest events (S0173a, S0235b, and S0325a) unobservable. Seismic monitoring conditions have improved again since sol 780 (February 2021), and we expect ~10 additional *P-S* travel-time observations during the extended mission. Meanwhile, our preliminary radial velocity model for the upper mantle of Mars will help to guide and inform searches for other seismic arrivals, particularly core-related phases [the core is considered in more detail in (*54*)]; possibly aid in aligning currently unlocated LF events to complement our dataset; and constrain a variety of geophysical and geochemical models as well as models of planetary evolution.

REFERENCES AND NOTES

1. W. B. Banerdt *et al.*, *Nat. Geosci.* **13**, 183–189 (2020).
2. M. Golombek *et al.*, *Nat. Commun.* **11**, 1014 (2020).
3. P. Lognonné *et al.*, *Space Sci. Rev.* **215**, 12 (2019).
4. P. Lognonné *et al.*, *Nat. Geosci.* **13**, 213–220 (2020).
5. D. Giardini *et al.*, *Nat. Geosci.* **13**, 205–212 (2020).
6. See supplementary materials.
7. J. F. Clinton *et al.*, *Phys. Earth Planet. Inter.* **310**, 106595 (2021).
8. H. Jeffreys, K. E. Bullen, *Seismological Tables* (British Association for the Advancement of Science, 1940).
9. A. M. Dziewonski, D. L. Anderson, *Phys. Earth Planet. Inter.* **25**, 297–356 (1981).
10. B. L. N. Kennett, E. R. Engdahl, *Geophys. J. Int.* **105**, 429–465 (1991).
11. A. Schaeffer, S. Lebedev, *Geophys. J. Int.* **194**, 417–449 (2013).
12. J. Ritsema, A. Deuss, H. J. van Heijst, J. H. Woodhouse, *Geophys. J. Int.* **184**, 1223–1236 (2011).
13. C. Nunn *et al.*, *Space Sci. Rev.* **216**, 89 (2020).
14. R. C. Weber, P.-Y. Lin, E. J. Garnero, Q. Williams, P. Lognonné, *Science* **331**, 309–312 (2011).
15. R. F. Garcia, J. Gagnepain-Beyneix, S. Chevrot, P. Lognonné, *Phys. Earth Planet. Inter.* **188**, 96–113 (2011).
16. R. F. Garcia *et al.*, *Space Sci. Rev.* **215**, 50 (2019).
17. M. P. Panning *et al.*, *Icarus* **248**, 230–242 (2015).
18. A. Khan *et al.*, *Phys. Earth Planet. Inter.* **258**, 28–42 (2016).
19. P. Lognonné *et al.*, *Planet. Space Sci.* **44**, 1237–1249 (1996).
20. F. Bissig *et al.*, *Space Sci. Rev.* **214**, 114 (2018).
21. InSight Marsquake Service, Mars Seismic Catalogue, InSight Mission; V4 2020-07-01. ETHZ, IPGP, JPL, ICL, ISAE-Supaero, MPS, University of Bristol Dataset (2020).
22. N. Brinkman *et al.*, *J. Geophys. Res. Planets* **126**, e2020JE006546 (2021).
23. M. Drilleau *et al.*, *Earth Space Sci.* **7**, e2020EA001118 (2020).
24. M. A. Wieczorek, M. T. Zuber, *J. Geophys. Res. Planets* **109**, E01009 (2004).
25. G. A. Neumann *et al.*, *J. Geophys. Res. Planets* **109**, E08002 (2004).
26. E. Bozdağ *et al.*, *Space Sci. Rev.* **211**, 571–594 (2017).
27. A. Khan *et al.*, *J. Geophys. Res. Planets* **123**, 575–611 (2018).
28. G. J. Taylor, *Geochemistry* **73**, 401–420 (2013).
29. J. A. D. Connolly, *Geochem. Geophys. Geosyst.* **10**, Q10014 (2009).
30. D. Breuer, T. Spohn, *J. Geophys. Res. Planets* **108**, 5072 (2003).
31. M. Thiriet, C. Michaut, D. Breuer, A.-C. Plesa, *J. Geophys. Res. Planets* **123**, 823–848 (2018).
32. H. Samuel, P. Lognonné, M. Panning, V. Lainey, *Nature* **569**, 523–527 (2019).
33. A.-C. Plesa *et al.*, *J. Geophys. Res. Planets* **121**, 2386–2403 (2016).
34. K. Mosegaard, A. Tarantola, *J. Geophys. Res. Solid Earth* **100**, 12431–12447 (1995).
35. A. Broquet, M. A. Wieczorek, W. Fa, *Geophys. Res. Lett.* **47**, e2019GL086746 (2020).
36. B. Knapmeyer-Endrun *et al.*, *Science* **373**, 438–443 (2021).
37. Y. Zheng, F. Nimmo, T. Lay, *Phys. Earth Planet. Inter.* **240**, 132–141 (2015).
38. S.-i. Karato, *Phys. Earth Planet. Inter.* **228**, 300–306 (2014).
39. C. J. Cline Ii, U. H. Faul, E. C. David, A. J. Berry, I. Jackson, *Nature* **555**, 355–358 (2018).
40. H. Kawakatsu, H. Utada, *Annu. Rev. Earth Planet. Sci.* **45**, 139–167 (2017).
41. T. Spohn, *Icarus* **90**, 222–236 (1991).
42. D. J. Stevenson, T. Spohn, G. Schubert, *Icarus* **54**, 466–489 (1983).
43. A. Morschhauser, M. Grott, D. Breuer, *Icarus* **212**, 541–558 (2011).
44. H. Wänke, G. Dreibus, *Philos. Trans. R. Soc. London Ser. A* **349**, 285–293 (1994).
45. T. Yoshizaki, W. F. McDonough, *Geochim. Cosmochim. Acta* **273**, 137–162 (2020).
46. J. Ruiz, V. López, J. M. Dohm, *Icarus* **207**, 631–637 (2010).
47. L. M. Parro, A. Jiménez-Díaz, F. Mansilla, J. Ruiz, *Sci. Rep.* **7**, 45629 (2017).
48. S. E. Smrekar *et al.*, *Space Sci. Rev.* **215**, 3 (2019).
49. H. Y. McSween Jr., G. J. Taylor, M. B. Wyatt, *Science* **324**, 736–739 (2009).
50. S. R. Taylor, S. M. McLennan, *Planetary Crusts: Their Composition, Origin and Evolution* (Cambridge Univ. Press, 2008).
51. G. J. Taylor *et al.*, *J. Geophys. Res. Planets* **111**, E03S10 (2006).
52. V. Sautter *et al.*, *Lithos* **254–255**, 36–52 (2016).
53. H. Y. McSween Jr., T. L. Grove, M. B. Wyatt, *J. Geophys. Res. Planets* **108**, 5135 (2003).
54. S. C. Stähler *et al.*, *Science* **373**, 443–448 (2021).
55. InSight Mars SEIS Data Service, SEIS raw data, Insight Mission. IPGP, JPL, CNES, ETHZ, ICL, MPS, ISAE-Supaero, LPG, MFSC (2019).
56. InSight Mars SEIS Data Service, InSight SEIS Data Bundle. PDS Geosciences (GEO) Node (2019).
57. InSight Marsquake Service, Mars Seismic Catalogue, InSight Mission; V4 2020-10-01 (2020).

Science

Upper mantle structure of Mars from InSight seismic data

Amir Khan, Savas Ceylan, Martin van Driel, Domenico Giardini, Philippe Lognonné, Henri Samuel, Nicholas C. Schmerr, Simon C. Stähler, Andrea C. Duran, Quancheng Huang, Doyeon Kim, Adrien Broquet, Constantinos Charalambous, John F. Clinton, Paul M. Davis, Mélanie Drilleau, Foivos Karakostas, Vedran Lekic, Scott M. McLennan, Ross R. Maguire, Chloé Michaut, Mark P. Panning, William T. Pike, Baptiste Pinot, Matthieu Plasman, John-Robert Scholz, Rudolf Widmer-Schnidrig, Tilman Spohn, Suzanne E. Smrekar and William B. Banerdt

Single seismometer structure

Because of the lack of direct seismic observations, the interior structure of Mars has been a mystery. Khan *et al.*, Knapmeyer-Endrun *et al.*, and Stähler *et al.* used recently detected marsquakes from the seismometer deployed during the InSight mission to map the interior of Mars (see the Perspective by Cottaar and Koelemeijer). Mars likely has a 24- to 72-kilometer-thick crust with a very deep lithosphere close to 500 kilometers. Similar to the Earth, a low-velocity layer probably exists beneath the lithosphere. The crust of Mars is likely highly enriched in radioactive elements that help to heat this layer at the expense of the interior. The core of Mars is liquid and large, ~1830 kilometers, which means that the mantle has only one rocky layer rather than two like the Earth has. These results provide a preliminary structure of Mars that helps to constrain the different theories explaining the chemistry and internal dynamics of the planet.
Science, abf2966, abf8966, abi7730, this issue p. 434, p. 438, p. 443 see also abj8914, p. 388

ARTICLE TOOLS	http://science.sciencemag.org/content/373/6553/434
SUPPLEMENTARY MATERIALS	http://science.sciencemag.org/content/suppl/2021/07/21/373.6553.434.DC1
RELATED CONTENT	http://science.sciencemag.org/content/sci/373/6553/388.full http://science.sciencemag.org/content/sci/373/6553/438.full http://science.sciencemag.org/content/sci/373/6553/443.full
REFERENCES	This article cites 89 articles, 13 of which you can access for free http://science.sciencemag.org/content/373/6553/434#BIBL
PERMISSIONS	http://www.sciencemag.org/help/reprints-and-permissions

Use of this article is subject to the Terms of Service